

Latent Graph Representations for Critical View of Safety Assessment

Aditya Murali, Deepak Alapatt, Pietro Mascagni, Armine Vardazaryan, Alain Garcia, Nariaki Okamoto, Didier Mutter, and Nicolas Padoy

Abstract—Assessing the critical view of safety in laparoscopic cholecystectomy requires accurate identification and localization of key anatomical structures, reasoning about their geometric relationships to one another, and determining the quality of their exposure. In this work, we propose to capture each of these aspects by modeling the surgical scene with a disentangled latent scene graph representation, which we can then process using a graph neural network. Unlike previous approaches using graph representations, we explicitly encode in our graphs semantic information such as object locations and shapes, class probabilities and visual features. We also incorporate an auxiliary image reconstruction objective to help train the latent graph representations. We demonstrate the value of these components through comprehensive ablation studies and achieve state-of-the-art results for critical view of safety prediction across multiple experimental settings.

Index Terms—Scene Graphs, Representation Learning, Surgical Scene Understanding, Critical View of Safety

I. INTRODUCTION

Surgical video analysis is a quickly expanding research direction with several promising applications such as automated surgical phase, gesture, and tool recognition/segmentation [1]–[4]. One key next step is to develop video-based methods for safety-critical applications. A few such applications have been proposed, including detection of critical or adverse events [5], [6] and intraoperative guidance via identification of safe actions or anatomical regions [7], [8]. A common thread among these applications is the increased importance of anatomy, and often times fine-grained anatomy. Go-NoGo Net [7], for instance, identifies regions of safe and unsafe dissection that are defined independently of surgical tool information, while Kolbinger et al. [8] explore automatic identification

This work was supported by French state funds managed by the ANR within the National AI Chair program under Grant ANR-20-CHIA-0029-01 (Chair AI4ORSafety) and within the Investments for the future program under Grants ANR-10-IDEX-0002-02 (IdEx Unistra) and ANR-10-IAHU-02 (IHU Strasbourg). This work was granted access to the HPC resources of IDRIS under the allocation 2021-AD011011640R1 made by GENCI.

Aditya Murali, Deepak Alapatt, and Nicolas Padoy are affiliated with ICube, University of Strasbourg, CNRS, France (email: {murali, alapatt, npadoy}@unistra.fr).

Pietro Mascagni, Armine Vardazaryan, Alain Garcia, Didier Mutter, and Nicolas Padoy are affiliated with IHU-Strasbourg, Institute of Image-Guided Surgery, Strasbourg, France.

Pietro Mascagni is affiliated with Fondazione Policlinico Universitario Agostino Gemelli IRCCS, Rome, Italy.

Nariaki Okamoto is affiliated with Institute for Research against Digestive Cancer (IRCAD), Strasbourg, France.

of dissection planes, which are similarly defined based on anatomy rather than surgical tools or surgeon activity. Yet, distinguishing anatomical structures is a difficult task as they are similar in color and texture and are highly deformable; to tackle this difficulty, these approaches rely on spatially dense annotations (e.g. segmentation masks), and while the resulting methods are effective, such annotations require clinical expertise and are difficult to collect and review.

Mascagni et al. [9] partially tackle this problem in their work on automatic identification of the critical view of safety (CVS), a clinically validated intervention that is associated with reduced rates of bile duct injury in laparoscopic cholecystectomy. To reduce annotation costs, they propose to annotate a subset of images with dense segmentation masks, which they bootstrap to generate pseudo-labels for the remainder of images. They show that passing the concatenation of the resulting masks and images to a deep learning model rather than the images alone enforces the model to condition CVS assessment on the hepatocystic anatomy, improving performance. In this work, we build on the previous approach, called DeepCVS, recognizing two main limitations. Firstly, the DeepCVS approach of concatenating an image with its segmentation mask to incorporate anatomical information (1) requires the model to learn to associate foreground objects with their visual properties, a redundant task given that it first predicts the segmentation mask from the image, and (2) allows extraneous visual information such as background textures to affect the downstream CVS predictions (see Fig. 1a). Secondly, DeepCVS is trained and validated on a small dataset of hand-picked frames, raising questions about its generalizability to real surgical scenarios.

To tackle the first limitation, inspired by recent works on object-centric representations [10]–[12], we propose to construct an anatomy-aware *latent graph representation* by using predicted semantic information (e.g. segmentation masks) to disentangle and re-structure the latent space of an image as a graph. The graph nodes contain the class information, location, and visual features of each anatomical structure, while the graph edges encode geometric and visual properties of the relationships between structures (see Fig. 1b). To ensure that the latent graphs effectively capture the anatomical configuration of the scene, we train them in a multi-task fashion, using dense labels (bounding boxes/segmentation masks) and an auxiliary reconstruction objective. We can then process the trained graphs with a graph neural network to predict CVS. As a result, in contrast to DeepCVS, our approach learns an

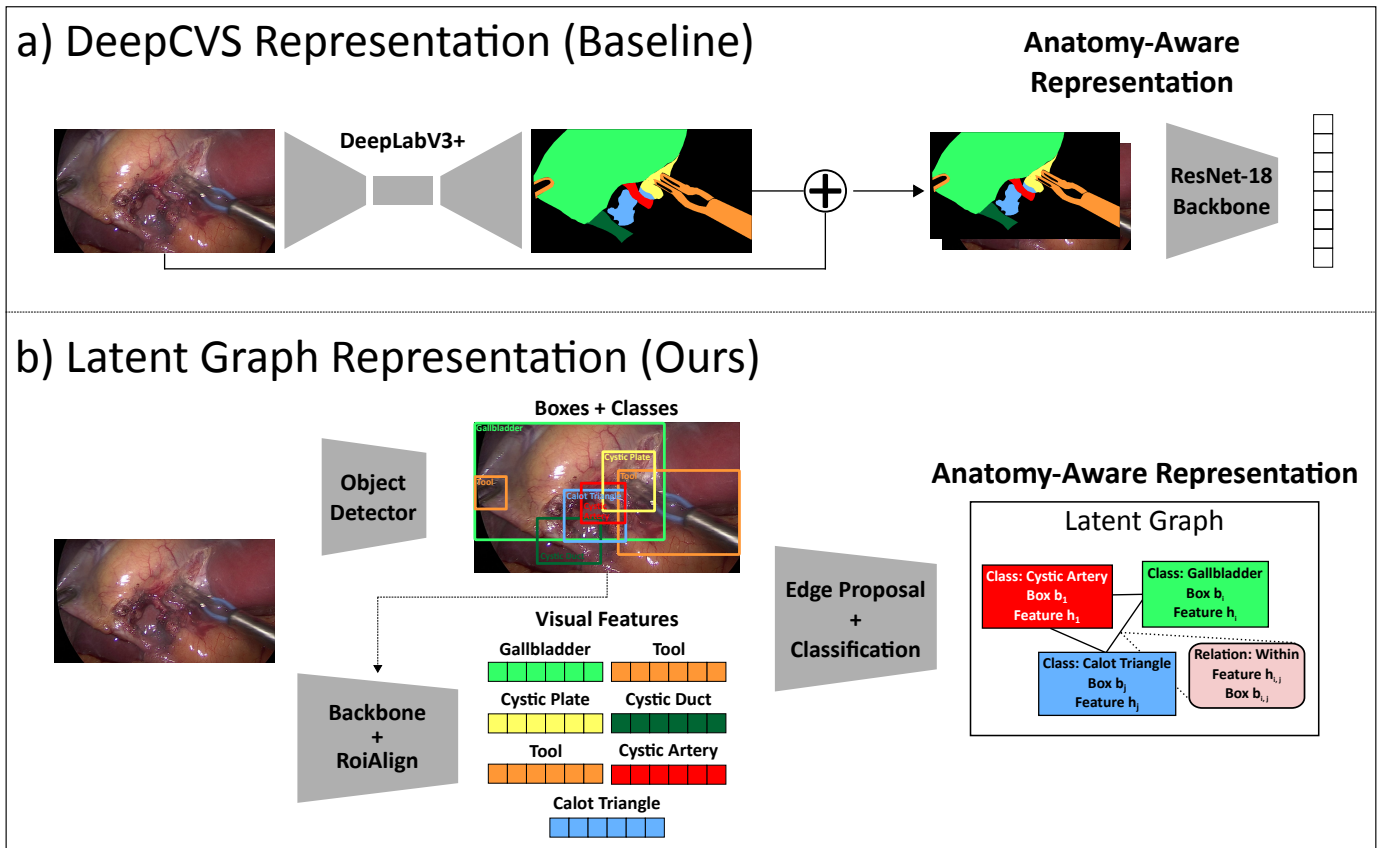


Fig. 1: Top: An illustration of the representation used in DeepCVS [9], which consists of an image concatenated with the corresponding predicted segmentation mask (See Sec. IV-A). Bottom: Our proposed latent graphical representation that represents the surgical scene based on the anatomical structures and tools as well as their bounding box locations and visual features.

anatomy-aware representation that ensures effective coupling of the visual and semantic properties of each foreground object, eliminates extraneous background information, and enables CVS prediction as a function of anatomy. Meanwhile, to address the dataset size limitation, we introduce a dataset with 5x as many images, segmentation masks, and CVS annotations as that of DeepCVS, while following the same strategy of only annotating a subset of the data with segmentation masks. Moreover, we sample and annotate frames at even intervals from each video in contrast with the DeepCVS dataset, which contains a collection of hand-picked frames. This requires methods to generalize to blur, poor views, and occlusions caused by tools, smoke, and bleeding, all of which naturally occur during a procedure.

In our experiments, we explore two evaluation settings: CVS prediction using segmentation masks, as used by DeepCVS, and CVS prediction using bounding boxes, representing different ground-truth availability scenarios. We additionally present extensions of the DeepCVS baseline that include an auxiliary reconstruction objective and work in the bounding box setting; we compare our method against these extensions, achieving state-of-the-art results for CVS prediction.

Our contributions can be summarized as follows:

- 1) We propose a novel anatomy-aware latent graph representation that summarizes a surgical scene by encoding the visual and semantic properties of each constituent

object and inter-object relation; this representation can be processed with a graph neural network architecture to predict CVS.

- 2) We show that an auxiliary reconstruction objective can improve performance and stability of CVS prediction performance across methods.
- 3) We introduce an expanded and more clinically representative dataset for CVS prediction with regularly spaced frames from 201 laparoscopic cholecystectomy procedures annotated independently by three experts.
- 4) We devise a comprehensive evaluation paradigm for CVS prediction comprising two experimental settings and demonstrate substantial performance improvements over strong baselines.

II. RELATED WORK

A. Scene Graphs

Scene graphs have been used in numerous fashions in the computer vision community. Initial works focused on scene graph generation from images [13]–[15] as an extension of object detection. Later works expanded these efforts to dynamic/spatio-temporal scene graph generation [16], [17], aggregating detected scene graphs across time, and 3D scene graph generation [18] augmenting the predicted scene graphs with properties such as object shapes and depth. These efforts have been translated to the surgical domain in a series of

works that focuses on scene graph prediction from a dataset of benchtop robotic surgery videos [19], [20], as well as a recent work predicting 4D (spatiotemporal, 3D) scene graphs describing operating room activity and workflow [21]. In parallel, numerous works have shown the value of scene graphs as input to various downstream tasks, primarily focusing on image generation. [22] and [23] describe approaches to generate images from scene graphs, first generating a scene layout from an input graph then using this layout to reconstruct the image. [24] extends this paradigm to image editing using scene graphs, augmenting the scene graphs with visual features extracted from the original image.

In a similar vein to [24], several works explore intermediate scene graph representations for various downstream tasks. In contrast to [24], they propose to structure the intermediate representation of an image or video clip in an object-centric or graphical form rather than augment a ground truth or predicted scene graph with visual features. [11] uses an intermediate graph representation for visual relationship detection, while [25] and [26] propose to improve scene graph prediction by including reconstruction and segmentation from the intermediate graph as auxiliary tasks. While these methods are primarily focused on improving the quality of the generated scene graphs or their components, [10] and [12] propose to use intermediate spatio-temporal graph representations for fine-grained action recognition; yet, these methods ignore semantic information in the graph representation, using only visual features. [27] partially addresses these limitations, showing the value of including semantics as well as visual features in the graph, but still ignores edge information. Similar end-to-end graphical approaches have also been proposed in the surgical domain: [28] constructs spatio-temporal graphs using surgical tool pose information to condition downstream surgical activity recognition on tool trajectories, but the resulting graphs discard the visual information in the scene; meanwhile, [29] constructs multi-modal graphs using video and kinematic information for downstream gesture recognition, but these graphs are coarse-grained and do not include object information, instead representing each input modality as a node.

In this work, we attempt to unify the findings of these works by identifying components that improve the quality of a fine-grained latent graph representation, measured by downstream task performance. Contrary to previous works with intermediate graph representations, we adopt a multi-task approach to train our latent graphs, using scene graph prediction, semantic segmentation, and image reconstruction as pretext tasks. In addition, inspired by [26], we introduce a segmentation grounding module to enhance the graph representation. We conduct comprehensive ablation studies that illustrate the impact of (1) these pretraining objectives and (2) encoding semantic properties such as class probabilities, bounding box coordinates, and segmentation masks in both the node and edge features.

B. Machine Learning for Surgical Safety Applications

Surgical workflow recognition from video is well-explored through tasks such as phase recognition, step detection, tool

detection/segmentation, and gesture recognition [1], [2], [30]–[32], with several works showing effective performance even in weakly supervised and unsupervised settings [33]–[37]. One missing component in these tasks is the explicit consideration of anatomy; to this end, several tasks have been introduced, including surgical triplet recognition, which involves decomposing surgical workflow into triplets of $\langle instrument, verb, target \rangle$ [38], and full scene segmentation [39]–[42].

Recent works have started to translate these ideas to safety-critical applications, which largely rely on effective anatomy recognition. The aforementioned [7] trains a neural network to identify safe and unsafe dissection zones (Go-NoGo zones) in laparoscopic cholecystectomy, while another recent work proposes a model for binary segmentation of critical structures (cystic artery and duct) [43], also in cholecystectomy. While these approaches are effective, their outputs are not yet clinically validated to correlate to safer outcomes; in contrast, the critical view of safety, first proposed in 1995 [44], has a long history of effectiveness, and is now included as a component of all major guidelines for safe laparoscopic cholecystectomy. To this end, Mascagni et al. proposed EndoDigest [45], an approach to automatically isolate the period of cystic duct division in cholecystectomy procedures followed by the aforementioned DeepCVS [9] for CVS prediction.

In this work, we present an improved methodology to incorporate anatomical information into the learning process by constructing an anatomy-aware latent graph representation processed with a graph neural network, focusing on CVS prediction as the downstream task.

III. METHODS

In this section, we begin by describing our expanded dataset for CVS prediction. Then we describe our latent graph encoder Φ_{LG} that generates a latent graph G from an image I (illustrated in Fig. 1b) and is trained in a multi-task fashion. Finally, we describe our two latent graph decoders: a reconstruction decoder $\phi_{\mathcal{R}}$ to help train the latent graphs and a CVS decoder ϕ_{CVS} to predict CVS (illustrated in Fig. 2).

A. Dataset

DeepCVS [9] utilizes a dataset of 2854 images that are hand-picked from 201 laparoscopic cholecystectomy videos. These images are annotated with achievement of each of the three CVS criteria, and a subset of 402 images are further annotated with semantic segmentation masks. As previously noted, this is not only a small dataset but also an unrealistic representation of a surgical procedure, as the frame selection process introduces bias. Alapatt et al. [42] tackle this problem in a follow-up work by introducing the Endoscapes dataset, which comprises 2208 frames selected at a regular interval (once every 30 seconds) from the same 201 videos and annotated with semantic segmentation masks. Because we are interested in CVS prediction, we further extend the Endoscapes dataset with CVS labels every 5 seconds, where CVS labels are vectors of three binary values corresponding to the three CVS criteria (C1, C2, C3 in Table I), and annotated by three independent and specifically trained surgeons following

TABLE I: CVS Achievement (%) by Criterion.

Criterion	Train	Val	Test
C1: Two Structures	15.6	16.3	24.0
C2: HCT Dissection	11.2	12.5	17.1
C3: Cystic Plate	17.9	16.7	27.1

the protocol of [46]. For the purposes of this work, we use segmentation masks with 7 classes, consisting of anatomical structures and a tool class, following [42].

From the segmentation masks, we additionally generate ground-truth bounding box and scene graph annotations (see Fig. 3) that we use to train our latent graph generation model. To generate bounding boxes, we take the semantic mask for each class and compute the smallest rectangular box that encloses the mask. Additionally, for the tool class, because we can have multiple instances, we include a connected components step which separates each tool instance¹. To generate scene graphs, inspired by [22], we assign one of three directional relationships between each pair of boxes based on their bounding box coordinates: {left-right, up-down, inside-outside}. Unlike [22] we use undirected edges rather than directed and select E edges per node by ranking edges using generalized intersection-over-union (gIoU) [47] between the two node bounding boxes; this ensures more consistent graphs, facilitating downstream graph classification.

Altogether, we have a dataset that is roughly 5x the scale of the dataset used in DeepCVS, comprising 11090 images with CVS annotations of which 1933 also have segmentation, bounding box, and synthetic scene graph annotations. For training and evaluation, we aggregate the three CVS annotations per image into a single ground-truth consensus vector by computing the mode for each criterion. Finally, we split the 201 videos into 120 training, 41 validation, and 40 testing, adopting the same split as [42]. Table I shows the proportion of frames in which each CVS criterion is achieved.

B. Latent Graph Encoder

To obtain the latent graph representation G of an image I , we pass the image through our latent graph encoder Φ_{LG} . Φ_{LG} consists of an object detector (augmented with a mask head when training with segmentation ground truth) to generate graph nodes, an edge proposal module to predict the graph structure, a segmentation grounding module to incorporate predicted masks into the latent graphs, and finally a graph neural network that updates node and edge features and classifies each edge. Following numerous scene graph generation works [11], [13], we train a MaskRCNN model for object detection/segmentation; this yields a set of N objects or nodes $\mathcal{O} = \{b_i, c_i, m_i \mid 1 \leq i \leq N\}$, where $b_i \in \mathbb{R}^4$ are box coordinates, $c_i \in [0, 1]^C$ are vectors of class probabilities with C object classes (including background), and $m_i \in \mathbb{R}^{M \times M}$ are instance masks. We then augment these detected objects

with visual features, taking the feature map of the image H and applying the *RoIAlign* operation from MaskRCNN to generate node features h_i . Concretely:

$$\begin{aligned} H &= \phi_{\text{backbone}}(I), \\ h_i &= \text{RoIAlign}(H, b_i), \end{aligned} \quad (1)$$

where ϕ_{backbone} is a ResNet50-FPN [48] backbone that is shared with the object detector and has an output channel size of $\mathcal{F}_{\text{backbone}}$. Combining the h_i with the b_i and c_i from the set of objects \mathcal{O} yields the initial graph nodes $\mathcal{N}^{\text{init}}$:

$$\mathcal{N}^{\text{init}} = \{b_i, c_i, h_i \mid 1 \leq k \leq N\}. \quad (2)$$

Edge Proposal. Once we have the graph nodes, the next step is to generate the graph structure by predicting the connectivity among nodes. To do so, we start with a fully connected graph, then score each edge using a learned function $\phi_{\text{edge_score}}$, then sample the highest scoring edges. We implement $\phi_{\text{edge_score}}$ as a Relation Proposal Network (RelPN) [13] that takes as input the predicted bounding box, class logits, and visual features for a pair of nodes i, j and outputs a scalar score $s_{i,j}$ for each edge (i, j) :

$$\begin{aligned} \phi_{\text{edge_score}} &: \mathbb{R}^{F_{\text{backbone}}+C+4} \times \mathbb{R}^{F_{\text{backbone}}+C+4} \mapsto \mathbb{R}^1, \\ x_i &= (b_i, c_i, h_i), \quad x_j = (b_j, c_j, h_j), \\ s_{i,j} &= \phi_{\text{edge_score}}(x_i, x_j). \end{aligned} \quad (3)$$

We then select the E highest scoring edges per node and drop duplicate edges (as G is undirected, this sampling process can generate duplicates), to yield edge indices $\mathcal{E}_I \subseteq [1, N] \times [1, N]$. Finally, for each edge, defined by the indices in \mathcal{E}_I , we compute a bounding box $b_{i,j}$, edge mask $\hat{m}_{i,j}$, and visual features $v_{i,j}$, yielding the initial graph edges $\mathcal{E}^{\text{init}}$:

$$\begin{aligned} b_{i,j} &= b_i \cup b_j, \quad \hat{m}_{i,j} = [\hat{m}_i; \hat{m}_j] \\ h_{i,j} &= \text{RoIAlign}(H, b_{i,j}), \\ \mathcal{E}^{\text{init}} &= \{e_{i,j} : [b_{i,j}; h_{i,j}] \mid (i, j) \in \mathcal{E}_I\}. \end{aligned} \quad (4)$$

To train $\phi_{\text{edge_score}}$, we assign ground-truth binary edge presence values $\ell_{\text{presence}}(e_{i,j})$ to each edge $e_{i,j}$ based on the gIoU between its bounding box $b_{i,j}$ and the closest ground truth edge bounding box:

$$\ell_{\text{presence}}(e_{i,j}) = \begin{cases} 1 & \text{if } \max_k \text{gIoU}(b_{i,j}, b_k^{\text{gt}}) \geq 0.5, \\ 0 & \text{otherwise.} \end{cases} \quad (5)$$

Segmentation Grounding. Because the initial formulation of the latent graph G only includes box coordinates, class probabilities, and visual features, training with the segmentation objective can only implicitly improve the representation’s quality through visual features that better capture fine-grained scene characteristics (e.g. object boundaries). To more explicitly incorporate segmentation information into G and strongly condition downstream CVS prediction, inspired by [26], we introduce a *segmentation grounding* module. We note that DeepCVS [9] incorporates segmentation information into its anatomy-aware representation at a global level by concatenating a mask with the image and processing with a CNN (see Fig. 1a). We follow a similar approach but instead incorporate the segmentation information at a *local*

¹In certain cases, the connected components algorithm fails to separate multiple instances because the masks of the instances overlap. In these cases, we annotate a single box for the overlapping instances.

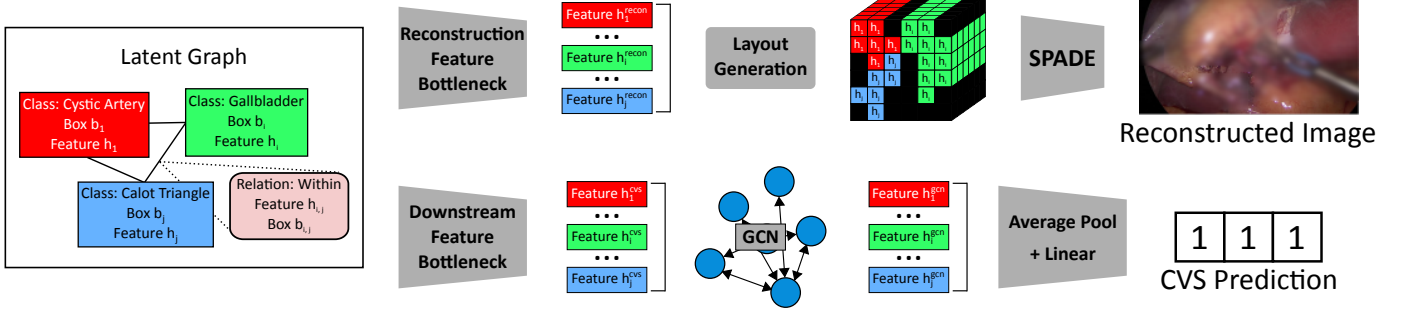


Fig. 2: The scene graph decoders $\phi_{\mathcal{R}}$ and ϕ_{CVS} to reconstruct an image and predict the CVS using the latent graph G .

level by concatenating the predicted instance mask of each node and edge (\hat{m}_i and $\hat{m}_{i,j}$) with the corresponding visual features (h_i and $h_{i,j}$) and passing the result through a shallow CNN, thereby maintaining disentanglement in our graphical representation. Concretely:

$$\begin{aligned} h_i^{\text{SG}} &= \phi_{\mathcal{N}}^{\text{SG}}([h_i; \hat{m}_i]), \\ h_{i,j}^{\text{SG}} &= \phi_{\mathcal{E}}^{\text{SG}}([h_{i,j}; \hat{m}_i; \hat{m}_j]), \end{aligned} \quad (6)$$

where $\phi_{\mathcal{N}}^{\text{SG}}$ and $\phi_{\mathcal{E}}^{\text{SG}}$ are 2-layer CNNs that output feature vectors of size F_{backbone}^2 . Last but not least, we update the visual features of the nodes $\mathcal{N}^{\text{init}}$ and edges $\mathcal{E}^{\text{init}}$ to the segmentation grounded features, yielding updated nodes \mathcal{N}^{SG} and edges \mathcal{E}^{SG} .

Edge Classification. Once we have our segmentation grounded graph (comprising \mathcal{N}^{SG} and \mathcal{E}^{SG}), we apply a 2-layer GNN, $\phi_{\text{LG-GNN}}$, to update the features of each node and edge based on the predicted graph structure. This step is critical for effective edge classification, as the union box $b_{i,j}$ and corresponding visual feature $h_{i,j}^{\text{SG}}$ are not always sufficient to properly assess the relation between nodes i and j , especially when training without segmentation masks. We adopt the GNN architecture of [24], which iteratively updates edge features and node features at each layer, and define the output dimension of $\phi_{\text{LG-GNN}}$ to be F_{backbone} . Applying $\phi_{\text{LG-GNN}}$ thus yields new node and edge features as follows:

$$\begin{aligned} H_{\text{node}}^{\text{LG}}, H_{\text{edge}}^{\text{LG}} &= \phi_{\text{LG-GNN}}(\mathcal{N}^{\text{SG}}, \mathcal{E}^{\text{SG}}), \text{ where} \\ H_{\text{node}}^{\text{LG}} &= \{h_i^{\text{LG}} \mid i \in [1, N]\} \text{ and } H_{\text{edge}}^{\text{LG}} = \{h_{i,j}^{\text{LG}} \mid (i, j) \in \mathcal{E}_I\}. \end{aligned} \quad (7)$$

We pass the updated edge features through $\phi_{\text{edge-classifier}}$, a 2-layer multi-layer perceptron (MLP) yielding predicted edge class logits as follows:

$$\begin{aligned} \phi_{\text{edge-classifier}} : \mathbb{R}^{F_{\text{backbone}}} &\mapsto \mathbb{R}^{C_E}, \\ c_{i,j} &= \phi_{\text{edge-classifier}}(h_{i,j}^{\text{LG}}), \end{aligned} \quad (8)$$

where C_E is the number of relation classes.

To train $\phi_{\text{edge-classifier}}$, we compute class labels for each edge following the same process as for ℓ_{presence} , but assign the ground truth class as the target for positive matches:

$$\ell_{\text{class}}(e_{i,j}) = \begin{cases} c_k^{\text{gt}} & \text{if } \max_k gIoU(b_{i,j}, b_k^{\text{gt}}) \geq 0.5, \\ 0 & \text{otherwise.} \end{cases} \quad (9)$$

²In the bounding box setting, we simply set $h_i^{\text{SG}} = h_i$ and $h_{i,j}^{\text{SG}} = h_{i,j}$.

Final Latent Graph Representation. Our final latent graph representation G is composed of the bounding boxes, class logits, and segmentation-grounded and GNN-processed visual features for each node and edge:

$$\begin{aligned} G &= \{\mathcal{N}^{\text{LG}}, \mathcal{E}^{\text{LG}}\}, \text{ where} \\ \mathcal{N}^{\text{LG}} &= \{(b_i, c_i, h_i^{\text{LG}} \mid i \in [1, N]\}, \text{ and} \\ \mathcal{E}^{\text{LG}} &= \{(b_{i,j}, c_{i,j}, h_{i,j}^{\text{LG}} \mid (i, j) \in \mathcal{E}_I\}. \end{aligned} \quad (10)$$

Figure 1b summarizes the process of generating a latent graph G from image I .

C. Latent Graph Decoders

We introduce two separate decoders that take the latent graph G as input: an image reconstruction decoder $\phi_{\mathcal{R}}$ and a CVS prediction decoder ϕ_{CVS} (see Fig. 2).

Image Reconstruction. Applying segmentation grounding and the latent graph GNN results in more expressive node and edge visual features; however, these are not supervised by the dense labels (bounding boxes/segmentation), and therefore lack a strong training signal. To address this problem, we introduce image reconstruction as an auxiliary task, generating an image \hat{I} from the latent graph G . We follow the method of [24], which first converts the predicted bounding boxes or instance masks into an image layout, then uses this image layout to spatially arrange the node features into a pixel-wise feature layout, and finally passes the feature layout to a SPADE [49] image reconstruction module $\phi_{\mathcal{R}}$ (see Fig. 2) to reconstruct the image. We compute the image layout L , which stores all nodes³ associated with a pixel (p_x, p_y) , as follows:

$$\begin{aligned} (x_1^i, y_1^i, x_2^i, y_2^i) &= b_i \\ L[p_x, p_y, i] &= \begin{cases} 1 & \text{if } x_1^i \leq p_x \leq x_2^i, \\ & y_1^i \leq p_y \leq y_2^i, \\ 0 & \text{otherwise.} \end{cases} \end{aligned} \quad (11)$$

When training the latent scene graphs with segmentation ground truth, we use each node's predicted binary instance mask \hat{m}_i rather than the predicted bounding box to generate L :

$$L[p_x, p_y, i] = \begin{cases} 1 & \text{if } \hat{m}_i[p_x, p_y] = i, \\ 0 & \text{otherwise.} \end{cases} \quad (12)$$

³When we are using predicted bounding boxes to generate L , we can have overlapping boxes, hence the need to account for multiple indices in some pixels.

Using the image layout L , we can compute the feature layout L_{feat} using the node visual features; here, we additionally apply a linear bottleneck $\mathcal{B}_{\mathcal{R}} : \mathbb{R}^{F_{\text{backbone}}} \mapsto \mathbb{R}^{F_{\mathcal{R}}}$ to the visual features to prevent the model from converging to a trivial solution. Altogether, we have:

$$\begin{aligned} h_i^{\mathcal{R}} &= \mathcal{B}_{\mathcal{R}}(h_i^{\text{LG}}), \\ L_{\text{feat}}[p_x, p_y] &= \sum_i L[p_x, p_y, i] * h_i^{\mathcal{R}}. \end{aligned} \quad (13)$$

To focus on the objects in the scene, we additionally incorporate a backgroundized image I_{bg} into the reconstruction input, generated by replacing all ground-truth bounding box regions with Gaussian noise; when ground-truth foreground is unavailable, we instead replace the predicted bounding box regions with noise. Finally, we concatenate L , L_{feat} , and I_{bg} and pass the result to $\phi_{\mathcal{R}}$, which outputs the reconstructed image \hat{I} .

CVS Prediction. To predict CVS from the latent graph, we use the CVS decoder ϕ_{CVS} (see Fig. 2), which is composed of a GNN (same architecture as $\phi_{\text{LG-GNN}}$) followed by a global pooling layer on the processed node features and a linear layer that outputs a vector of three values, corresponding to predicted scores for each CVS criterion. Similarly to the image reconstruction decoding process, we apply feature bottlenecks $\mathcal{B}_{\text{CVS}}^{\mathcal{N}} : \mathbb{R}^{F_{\text{backbone}}} \mapsto \mathbb{R}^{F_{\mathcal{N}}}$, and $\mathcal{B}_{\text{CVS}}^{\mathcal{E}} : \mathbb{R}^{F_{\text{backbone}}} \mapsto \mathbb{R}^{F_{\mathcal{E}}}$ to the node and edge visual features before evaluating ϕ_{CVS} .

D. Training Process

We train our model in 2 stages. In the first stage, we train the latent graph encoder Φ_{LG} jointly with the reconstruction decoder $\phi_{\mathcal{R}}$ using object detection/semantic segmentation, scene graph prediction, and image reconstruction objectives, enabling appropriate supervision for all constituents of Φ_{LG} . The overall loss function for the first stage is as follows:

$$\mathcal{L}_1 = \mathcal{L}_{\text{object_detector}} + \mathcal{L}_{\text{RelPN}} + \mathcal{L}_{\text{edge_classifier}} + \mathcal{L}_{\text{reconstruction}}, \quad (14)$$

where $\mathcal{L}_{\text{object_detector}}$ is the composite MaskRCNN loss, $\mathcal{L}_{\text{RelPN}}$ is a binary cross entropy loss following [13], $\mathcal{L}_{\text{edge_classifier}}$ is the cross entropy loss between predicted relations and matched ground truth relations, and finally $\mathcal{L}_{\text{reconstruction}}$ is the sum of the L1 Loss, Perceptual Similarity Loss [50], and Structural Similarity loss [51] between the original and reconstructed images.

In the second stage, we freeze the weights of Φ_{LG} and $\phi_{\mathcal{R}}$ and only train the CVS decoder ϕ_{CVS} . To handle the multi-label classification task and tackle the considerable class imbalance in the dataset (see Sec. III-A), we use a weighted binary cross entropy loss function \mathcal{L}_{CVS} , with loss weights given by median frequency balancing.

Box Perturbation. During the second stage of training, we use the entire training dataset rather than just the subset annotated with dense labels, since we only require ground-truth CVS annotations to train ϕ_{CVS} . As a result, our computed latent graph representations G are prone to semantic errors (missed objects, incorrectly localized objects, etc.), especially on these newly introduced images. To help increase robustness to these errors, we randomly perturb the box coordinates of

each node and edge in G during training. Specifically, we add a random noise vector $p_i = \lambda_{\text{perturb}} * (p_x^1, p_y^1, p_x^2, p_y^2)$ to each box b_i , where the p_x are drawn from a uniform distribution $U(-w, w)$, and the p_y from $U(-h, h)$, where h, w are the height and width of b_i . We show the impact of this box perturbation on CVS prediction and investigate the impact of the perturbation factor λ_{perturb} in Section IV-C.

IV. EXPERIMENTS AND RESULTS

A. Baseline Models

DeepCVS [9], the state-of-the-art method for CVS prediction, first passes images through a DeepLabV3+ model to predict segmentation masks, then concatenates the predicted masks with the original images and passes the result to a custom 6-layer network to predict the CVS (see Fig. 1a). Because we are not as severely constrained by dataset size, we note that different architectures may be better suited for this downstream classification task. To this end, we investigate replacing the original classification head from DeepCVS with MobileNetV3+, ResNet-18, and ResNet-50 architectures (see Table II), modifying the initial layer to ingest a 4-channel input (image and mask). We train each variant on our expanded dataset and find that the adapted ResNet-18 architecture achieves much improved performance compared to the original custom architecture. We proceed to use this variant of DeepCVS for our main experiments.

Algorithm 1 Bounding Boxes to Instance Mask Format

```

 $M^{\text{box}} \leftarrow \text{ZEROS}(H, W)$ 
for  $b_i, c_i \in B, C$  do
   $m_i^{\text{box}} \leftarrow \text{ZEROS}(H, W)$ 
   $(x_1, y_1, x_2, y_2) \leftarrow b_i$ 
   $m_i^{\text{box}}[y_1 : y_2, x_1 : x_2] \leftarrow c_i$ 
   $M^{\text{box}} \leftarrow M^{\text{box}} + m_i^{\text{box}}$ 
end for

```

DeepCVS with Bounding Boxes. We experiment with using both bounding boxes and instance segmentation masks as dense spatial labels to aid CVS prediction. To enable fair comparisons, we implement an extension of DeepCVS that uses predicted bounding boxes rather than segmentation masks by replacing the DeepLabV3+ segmentation model with a MaskRCNN object detector trained on the densely labeled data subset (same as in Sec. III-B). This yields predicted bounding boxes that we convert to instance masks with the same spatial dimensions as the input image. We can then collapse the set of instance masks into a single channel mask that we concatenate with the original image to predict the CVS. Algorithm 1

TABLE II: CVS Prediction Performance of DeepCVS Variants.

Architecture	CVS mAP
DeepCVS	54.18
DeepCVS-MobileNetV3+	57.53
DeepCVS-ResNet18	59.13
DeepCVS-ResNet50	58.76

TABLE III: CVS Prediction Performance of LatentGraph-CVS (ours) vs. DeepCVS

Dense Labels	Uses Recon	Method	Scene Graph Prediction	Obj Det	Seg	Reconstruction		CVS Criteria Prediction
			Recall @10	mAP@50	Macro F1	SSIM		mAP
						Overall	Rof	
Box	No	DeepCVS-ResNet18	-	53.47 ± 0.63	-	-	-	51.19 ± 1.77
		<i>LatentGraph-CVS (ours)</i>	46.24 ± 1.43	53.47 ± 0.63	-	-	-	57.15 ± 2.00
	Yes	DeepCVS-ResNet18	-	53.47 ± 0.63	-	62.28 ± 1.18	24.35 ± 0.42	54.12 ± 1.54
		<i>LatentGraph-CVS (ours)</i>	48.56 ± 0.12	54.82 ± 0.40	-	71.43 ± 0.32	38.23 ± 0.26	59.35 ± 0.36
Seg	No	DeepCVS-ResNet18	-	-	71.50 ± 0.44	-	-	59.13 ± 1.42
		<i>LatentGraph-CVS (ours)</i>	49.78 ± 0.68	-	71.67 ± 0.62	-	-	58.93 ± 2.34
	Yes	DeepCVS-ResNet18	-	-	71.50 ± 0.44	67.96 ± 0.83	34.16 ± 0.78	60.12 ± 1.09
		<i>LatentGraph-CVS (ours)</i>	50.51 ± 0.86	-	71.09 ± 0.64	76.08 ± 0.19	53.29 ± 0.34	61.33 ± 1.35

describes this process concretely, starting from the set of predicted bounding boxes B and predicted classes C for image I and ending up with a mask representation of the boxes M^{box} .

Algorithm 2 DeepCVS Reconstruction Decoder

$$\begin{aligned}
 H^{\text{DeepCVS}} &\leftarrow \mathcal{B}_{\text{DeepCVS}} \left(\phi_{\text{backbone}}^{\text{DeepCVS}} (\text{CONCAT}(I, M)) \right) \\
 L_{\text{feat}}^{\text{DeepCVS}} &\leftarrow \text{ZEROS}(S, H, W) \\
 L_{\text{feat}}^{\text{DeepCVS}}[:, M \neq 0] &\leftarrow H^{\text{DeepCVS}} \triangleright \text{foreground} \leftarrow \text{img feat} \\
 I_{\text{bg}} &\leftarrow I; I_{\text{bg}}[:, M^{\text{box}} \neq 0] \leftarrow 0 \triangleright \text{foreground} \leftarrow \text{noise} \\
 \hat{I} &\leftarrow \phi_{\mathcal{R}} \left(\text{CONCAT}(M^{\text{box}}, L_{\text{feat}}^{\text{DeepCVS}}, I_{\text{bg}}) \right)
 \end{aligned}$$

DeepCVS with Reconstruction. One major component of our training process is a reconstruction objective to help train Φ_{LG} . We note that such an objective can also improve the DeepCVS baseline by enforcing its anatomy-aware representation (see Fig. 1a) to include visual information, preventing over-reliance on semantics. To augment DeepCVS with a reconstruction objective, we use its anatomy-aware representation along with the predicted segmentation mask to generate a feature-augmented layout that we then pass to a reconstruction module $\phi_{\mathcal{R}}$, along with a backgroundized image I_{bg} , both defined as in Sec. III-C. We apply a linear bottleneck $\mathcal{B}^{\text{DeepCVS}}$ to the anatomy-aware representation to ensure fair comparisons with our LG-CVS model. The bottleneck size can be computed as $S = N * F_N$, such that S matches the total size of the latent graph G in our method. Because our goal is to improve the anatomy-aware representation, we continue to freeze the weights of the segmentation/object detection model, only training the downstream ResNet-18 model. Algorithm 2 describes this reconstruction formulation concretely.

B. CVS Prediction

We evaluate both our method and the DeepCVS baseline on our test set (see Sec. III-A) in two experimental settings: using bounding boxes vs. segmentation masks as the spatially dense labels. For each setting, we additionally present results with and without the auxiliary reconstruction objective.

Metrics. We present results for 5 total tasks in Table III, reporting mean and standard deviation across 3 randomly seeded

TABLE IV: Detailed Comparison of DeepCVS and LG-CVS (mAP is Mean Average Precision, Bacc is Balanced Accuracy).

		DeepCVS	LG-CVS
mAP	C1	65.91	63.54
	C2	52.60	54.65
	C3	61.84	65.78
	Avg	60.12	61.33
Bacc	C1	73.99	71.59
	C2	73.41	74.35
	C3	70.74	72.49
	Avg	72.27	72.81

runs: scene graph prediction (Scene Graph Recall@10 [15]), object detection (mAP₅₀), semantic segmentation (Macro F1), image reconstruction (structural similarity index, overall image and inpainted regions), and CVS Criteria prediction (average of per-criterion mean average precision). We retrain all MaskRCNN components for each variant of LatentGraph-CVS (LG-CVS Box, LG-CVS Box + Reconstruction, etc.), resulting in minor performance differences in the auxiliary task performances. In contrast, for the DeepCVS baselines, as described in IV-A, we use the same frozen pre-trained models.

Our LG-CVS is particularly effective in the bounding box setting, achieving an improvement of **7.73** mAP over the original DeepCVS baseline, and **4.8** mAP over our augmented baseline (DeepCVS with reconstruction). We also outperform DeepCVS in the segmentation setting, albeit with smaller improvements of **2.2** mAP over the original baseline and **1.21** mAP over our augmented baseline. These results highlight the reliance of DeepCVS on semantic information, as its performance sharply degrades in the bounding box setting, where this information is unavailable or not as precise. In contrast, our method effectively fuses semantic and visual properties of each anatomical structure in its anatomy-aware latent representation, and consequently, can use the visual information to improve downstream performance when the semantic information is imprecise. As a result, LG-CVS trained with bounding boxes only declines by **1.98** mAP points compared to LG-CVS trained with segmentation, and even achieves a minor improvement of **0.22** mAP over the original DeepCVS baseline (no reconstruction) with far lower

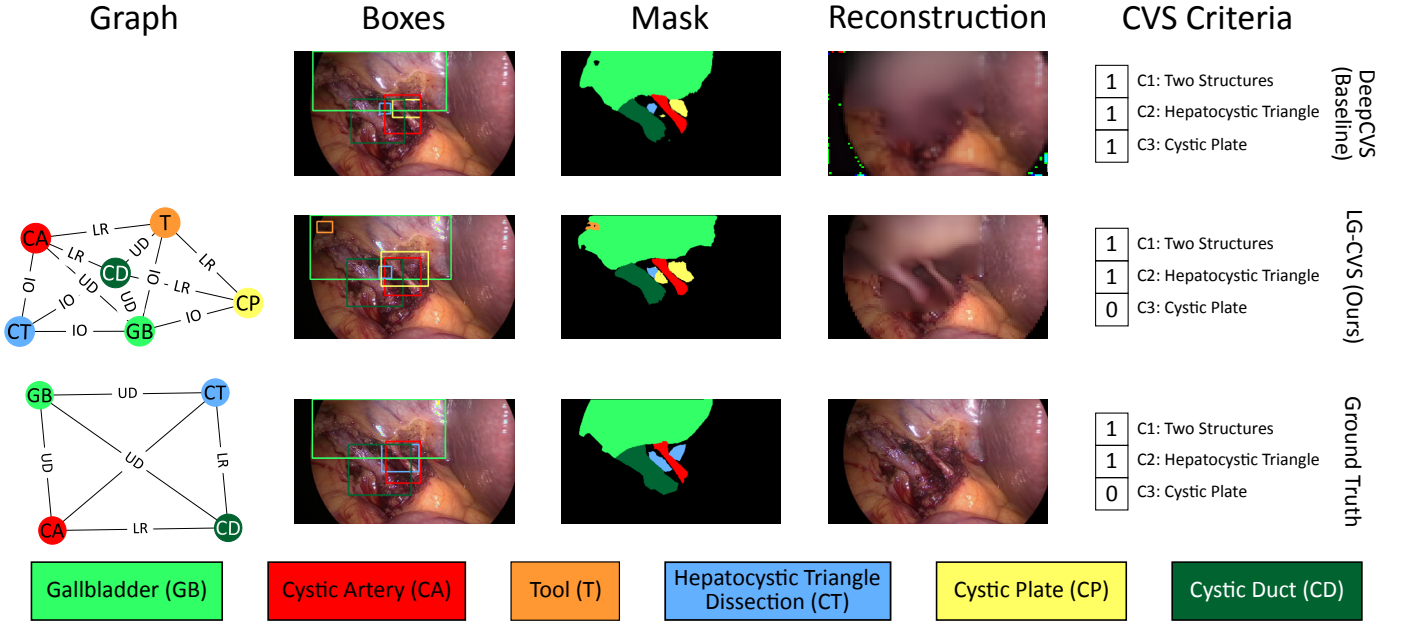


Fig. 3: Qualitative performance of the DeepCVS baseline (Top) vs. our LG-CVS method (Middle) on scene graph prediction, object detection, segmentation, reconstruction, and CVS prediction. In the predicted and ground truth graph, the relation labels are shortened as follows: LR = left-right, UD = up-down, IO = inside-outside. Note that DeepCVS does not perform scene graph prediction, so we omit this visualization.

annotation cost. Importantly, this effective feature fusion is still beneficial in the segmentation setting, where predicted masks are sometimes characterized by errors that our model can rectify using visual information.

Impact of Reconstruction Objective. As shown in Table III, including an auxiliary reconstruction objective improves CVS prediction performance of both the DeepCVS baseline (improvements of **2.97**, **0.99** mAP respectively in Box and Seg settings) and our LG-CVS (improvements of **2.20**, **2.40** mAP respectively in Box and Seg settings). This is due to the reconstruction objective forcing the respective anatomy-aware representations to better encode visual information; in the case of DeepCVS, it helps prevent the aforementioned over-reliance on semantics, while for the LG-CVS baseline, it ensures that the GNN-processed node and edge visual features (h_i^{LG} and $h_{i,j}^{LG}$) are properly grounded to their original corresponding objects/relations (see Sec. III-C).

Of note, in both experimental settings, the image reconstruction performance of DeepCVS is considerably lower than that of our LG-CVS, despite the fact that both methods use an identical intermediate representation size. Figure 3 qualitatively illustrates this phenomenon - whereas the DeepCVS reconstruction is uniformly blurry, our method’s reconstruction delineates the anatomical structures (cystic artery, cystic duct, hepatocystic triangle). This reinforces the notion that our disentangled latent graph representation more efficiently captures the anatomy of a scene (both visual and semantic properties) than the DeepCVS representation, even though both methods are trained with a reconstruction objective that includes a backgroundized image as input to focus the representation on the anatomical structures.

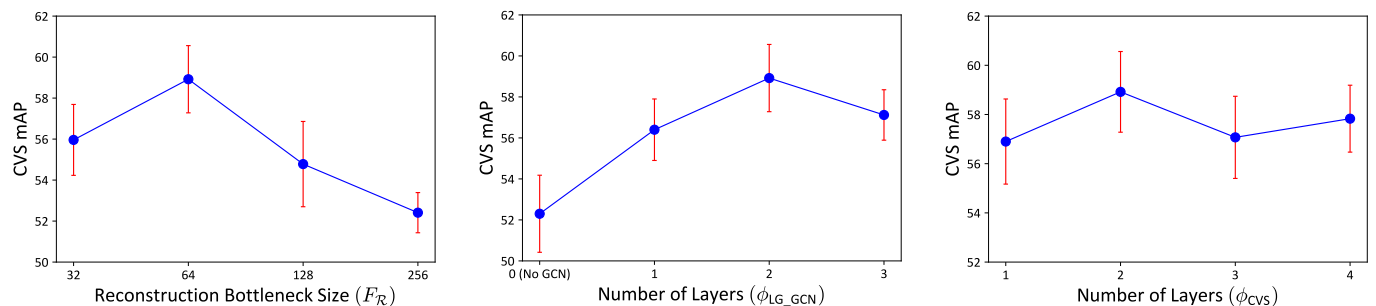
Criterion-Wise Performance. Table IV shows the component-wise performance of our LG-CVS model and the best DeepCVS model (DeepCVS with Reconstruction) in the

segmentation setting. Our model improves the classification performance for C2 (Hepatocystic Triangle Dissection) by **2.05** mAP and C3 (Cystic Plate) by **3.94**. These improvements are consistent with the design of our model: C2 and C3 classification rely on accurate detection and reasoning about the hepatocystic triangle and cystic plate; however, both our object detection and segmentation models are particularly error-prone for these classes. Yet, because our model more effectively includes visual information in its representation, it is better able to recover from such errors. In addition, our graph-based approach allows reasoning about the overall anatomical configuration in a scene, which can further improve robustness to detection errors. At the same time, we observe a decline of **2.47** mAP for C1 (Two Structures) classification; this could be a result of the visual information acting as a confounding factor. Fig. 3 illustrates this phenomenon: in both cases, the predicted boxes and masks are characterized by errors, most notably the incorrect detection of the cystic plate class. While the DeepCVS baseline incorrectly predicts the cystic plate criterion (C3) as achieved, our method correctly classifies all CVS components.

C. Ablation Studies

We additionally study the effect of various parameter settings on both the latent graph encoder Φ_{LG} and downstream CVS prediction. For brevity, we show the results of the ablations for the bounding box experimental setting, except for the segmentation grounding ablation, which only applies when training with segmentation ground truth. As with the main experiments in Sec. IV-B, we report performance statistics across 3 randomly seeded runs.

Latent Graph Components. The latent graph nodes and edges are composed of box coordinates, class logits, and visual



(a) Effect of Reconstruction Bottleneck Size $F_{\mathcal{R}}$ on downstream CVS performance. (b) Effect of GNN Layers in $\phi_{\text{LG-GNN}}$ on downstream CVS performance. (c) Effect of GNN Layers in ϕ_{CVS} on downstream CVS performance.

Fig. 4: A series of plots showing the effect of various hyperparameters on CVS prediction performance. Error bars show standard deviation.

TABLE V: Latent Graph Components Ablation Study.

Visual Features	Box Coordinates	Class Probabilities	CVS mAP
✗	✓	✓	55.27 ± 0.89
✓	✗	✗	56.50 ± 1.20
✓	✓	✗	55.20 ± 1.10
✓	✗	✓	57.37 ± 0.80
✓	✓	✓	59.35 ± 0.36

TABLE VI: Impact of Segmentation Grounding.

Segmentation Grounding	CVS mAP
✗	59.61 ± 1.60
✓	61.33 ± 1.35

features. Table V shows downstream CVS prediction performance when including various combinations of these components in G . Several prior works with intermediate graphical representations [10]–[12] only include visual features to represent nodes and edges; however, we observe an improvement of **2.85** mAP when additionally including box coordinates and class probabilities, demonstrating their importance in the latent graph. We also observe a decrease of **4.08** mAP when only including semantic information in the graph, which is almost the same as the DeepCVS baseline (difference of **1.08** mAP). This shows that our LG-CVS method synergistically combines semantic and visual information to predict CVS while the DeepCVS baseline is overly reliant on semantics.

Table VI shows the impact of the segmentation grounding module described in III-D. The performance without segmentation grounding is almost the same as LG-CVS with bounding boxes (difference of **0.26** mAP), underlining the importance of explicitly encoding segmentation information into the latent graphs.

Reconstruction Bottleneck Size. Prior to evaluating $\phi_{\mathcal{R}}$, we bottleneck the node visual features ($\phi_{\mathcal{R}}$ ignores the edge features) to prevent trivial solutions; this step ensures that the reconstruction objective helps the model learn a more powerful latent graph representation G . Figure 4a illustrates the impact of varying the bottleneck size $F_{\mathcal{R}}$ on the quality of the learned representation, reflected by the downstream CVS performance.

We find that setting $F_{\mathcal{R}} = 64$ yields the best performing model.

GNN Layers. Figures 4b and 4c investigate the impact of the number of GNN layers both in $\phi_{\text{LG-GNN}}$ and ϕ_{CVS} . We note that removing the latent graph GNN $\phi_{\text{LG-GNN}}$ severely degrades performance (7.05 mAP); this is primarily because edge classification without $\phi_{\text{LG-GNN}}$ is highly error-prone (see Sec. III-B, and underlines the importance of $\phi_{\text{LG-GNN}}$ in our method. We find that a 2-layer GNN architecture is most effective for both $\phi_{\text{LG-GNN}}$ and ϕ_{CVS} .

D. Implementation Details

We train all models on a single 32GB Nvidia V100 GPU, resizing all images from their original resolution of 480×854 to 240×427 . In the first stage, we train for 150 epochs, using a batch size of 32 and an Adam optimizer with a learning rate of 0.0001, using mAP₅₀ (bounding box experiments) or Macro F1 (segmentation experiments) score for model selection. In the second stage, we freeze the latent graph encoder of the selected model and train for 20 epochs using a batch size of 64 and an Adam optimizer with learning rate 0.0003, using validation mAP for model selection. Lastly, we include GraphNorm [52] and skip connections in $\phi_{\text{LG-GNN}}$ and ϕ_{CVS} .

V. CONCLUSION

In this work, we introduce anatomy-aware latent graph representations that can be used for anatomy-reliant tasks such as Critical View of Safety prediction. Our graph representations explicitly encode node and edge semantics, incorporate segmentation information via a grounding module, and can be trained in a multi-task fashion. In our experiments, we introduce a comprehensive CVS prediction evaluation paradigm considering different ground truth data availability scenarios and develop multiple extensions of the state-of-the-art DeepCVS baseline to ensure fair comparisons. We demonstrate that our method comprehensively outperforms these baselines, and also show that incorporating an auxiliary image reconstruction objective improves CVS prediction performance across methods. We believe that this work can serve as a template for approaching anatomy-reliant surgical video analysis tasks and promote future work exploring the use of graphical representations.

REFERENCES

- [1] I. Funke, S. Bodenstedt, F. Oehme, F. von Bechtolsheim *et al.*, “Using 3D convolutional neural networks to learn spatiotemporal features for automatic surgical gesture recognition in video,” in *MICCAI*, 2019.
- [2] Y. Jin, Q. Dou, H. Chen, L. Yu *et al.*, “Sv-rcnet: workflow recognition from surgical videos using recurrent convolutional network,” *IEEE transactions on medical imaging*, vol. 37, no. 5, pp. 1114–1126, 2017.
- [3] L. Maier-Hein, S. S. Vedula, S. Speidel, N. Navab *et al.*, “Surgical data science for next-generation interventions,” *Nature Biomedical Engineering*, vol. 1, no. 9, pp. 691–696, Sep. 2017.
- [4] Y. Jin, K. Cheng, Q. Dou, and P.-A. Heng, “Incorporating temporal prior from motion flow for instrument segmentation in minimally invasive surgery video,” in *MICCAI*. Springer, 2019, pp. 440–448.
- [5] H. Wei, F. Rudzicz, D. Fleet, T. Grantcharov *et al.*, “Intraoperative adverse event detection in laparoscopic surgery: Stabilized multi-stage temporal convolutional network with focal-uncertainty loss,” in *Machine Learning for Healthcare Conference*. PMLR, 2021, pp. 283–307.
- [6] T. Yu, P. Mascagni, J. Verde, J. Marescaux *et al.*, “Live laparoscopic video retrieval with compressed uncertainty,” *arXiv preprint arXiv:2203.04301*, 2022.
- [7] A. Madani, B. Namazi, M. S. Altieri, D. A. Hashimoto *et al.*, “Artificial intelligence for intraoperative guidance: using semantic segmentation to identify surgical anatomy during laparoscopic cholecystectomy,” *Annals of surgery*, 2022.
- [8] F. R. Kolbinger, S. Leger, M. Carstens, F. M. Rinner *et al.*, “Artificial intelligence for context-aware surgical guidance in complex robot-assisted oncological procedures: an exploratory feasibility study,” *medRxiv*, 2022.
- [9] P. Mascagni, A. Vardazaryan, D. Alapatt, T. Urade *et al.*, “Artificial intelligence for surgical safety: automatic assessment of the critical view of safety in laparoscopic cholecystectomy using deep learning,” *Annals of Surgery*, 2021.
- [10] X. Wang and A. Gupta, “Videos as space-time region graphs,” in *ECCV*, 2018, pp. 399–417.
- [11] M. Raboh, R. Herzig, J. Berant, G. Chechik *et al.*, “Differentiable scene graphs,” in *Proceedings of the IEEE/CVF Winter Conference on Applications of Computer Vision*, 2020, pp. 1488–1497.
- [12] S. Khan and F. Cuzzolin, “Spatiotemporal deformable scene graphs for complex activity detection,” *BMVC*, 2021.
- [13] J. Yang, J. Lu, S. Lee, D. Batra *et al.*, “Graph r-cnn for scene graph generation,” in *ECCV*, 2018, pp. 670–685.
- [14] R. Zellers, M. Yatskar, S. Thomson, and Y. Choi, “Neural motifs: Scene graph parsing with global context,” in *CVPR*, 2018, pp. 5831–5840.
- [15] C. Lu, R. Krishna, M. Bernstein, and L. Fei-Fei, “Visual relationship detection with language priors,” in *ECCV*. Springer, 2016, pp. 852–869.
- [16] J. Ji, R. Krishna, L. Fei-Fei, and J. C. Niebles, “Action genome: Actions as compositions of spatio-temporal scene graphs,” in *CVPR*, June 2020.
- [17] Y. Cong, W. Liao, H. Ackermann, B. Rosenhahn *et al.*, “Spatial-temporal transformer for dynamic scene graph generation,” in *ICCV*, October 2021, pp. 16 372–16 382.
- [18] S.-C. Wu, J. Wald, K. Tateno, N. Navab *et al.*, “Scenegrphfusion: Incremental 3d scene graph prediction from rgb-d sequences,” in *CVPR*, June 2021, pp. 7515–7525.
- [19] M. Islam, L. Seenivasan, L. C. Ming, and H. Ren, “Learning and reasoning with the graph structure representation in robotic surgery,” in *MICCAI*. Springer, 2020, pp. 627–636.
- [20] L. Seenivasan, S. Mitheran, M. Islam, and H. Ren, “Global-reasoned multi-task learning model for surgical scene understanding,” *IEEE Robotics and Automation Letters*, vol. 7, no. 2, pp. 3858–3865, 2022.
- [21] E. Özsoy, E. P. Örnek, U. Eck, T. Czempel *et al.*, “4d-or: Semantic scene graphs for or domain modeling,” *arXiv preprint arXiv:2203.11937*, 2022.
- [22] J. Johnson, A. Gupta, and L. Fei-Fei, “Image generation from scene graphs,” in *CVPR*, 2018, pp. 1219–1228.
- [23] A. Farshad, S. Musatian, H. Dharmo, and N. Navab, “Migs: Meta image generation from scene graphs,” *BMVC*, 2021.
- [24] H. Dharmo, A. Farshad, I. Laina, N. Navab *et al.*, “Semantic image manipulation using scene graphs,” in *CVPR*, 2020, pp. 5213–5222.
- [25] J. Gu, H. Zhao, Z. Lin, S. Li *et al.*, “Scene graph generation with external knowledge and image reconstruction,” in *CVPR*, June 2019.
- [26] S. Khandelwal, M. Suhaail, and L. Sigal, “Segmentation-grounded scene graph generation,” in *ICCV*, October 2021, pp. 15 879–15 889.
- [27] J. Materzynska, T. Xiao, R. Herzig, H. Xu *et al.*, “Something-else: Compositional action recognition with spatial-temporal interaction networks,” in *CVPR*, 2020, pp. 1049–1059.
- [28] D. Sarikaya and P. Jannin, “Towards generalizable surgical activity recognition using spatial temporal graph convolutional networks,” *arXiv preprint arXiv:2001.03728*, 2020.
- [29] Y. Long, J. Y. Wu, B. Lu, Y. Jin *et al.*, “Relational graph learning on visual and kinematics embeddings for accurate gesture recognition in robotic surgery,” in *ICRA*, 2021, pp. 13 346–13 353.
- [30] O. Zisimopoulos, E. Flouty, I. Luengo, P. Giataganas *et al.*, “Deepphase: surgical phase recognition in cataracts videos,” in *MICCAI*. Springer, 2018, pp. 265–272.
- [31] T. Czempiel, M. Paschali, M. Keicher, W. Simson *et al.*, “Tecno: Surgical phase recognition with multi-stage temporal convolutional networks,” in *MICCAI*. Springer, 2020, pp. 343–352.
- [32] S. Ramesh, D. Dall’Alba, C. Gonzalez, T. Yu *et al.*, “Multi-task temporal convolutional networks for joint recognition of surgical phases and steps in gastric bypass procedures,” *IJCARS*, vol. 16, no. 7, 2021.
- [33] D. Liu, Y. Wei, T. Jiang, Y. Wang *et al.*, “Unsupervised surgical instrument segmentation via anchor generation and semantic diffusion,” in *MICCAI*. Springer, 2020, pp. 657–667.
- [34] L. Sestini, B. Rosa, E. De Momi, G. Ferrigno *et al.*, “Fun-sis: a fully unsupervised approach for surgical instrument segmentation,” *arXiv preprint arXiv:2202.08141*, 2022.
- [35] J. Y. Wu, A. Tamhane, P. Kazanizides, and M. Unberath, “Cross-modal self-supervised representation learning for gesture and skill recognition in robotic surgery,” *IJCARS*, vol. 16, no. 5, pp. 779–787, 2021.
- [36] X. Shi, Y. Jin, Q. Dou, and P.-A. Heng, “Semi-supervised learning with progressive unlabeled data excavation for label-efficient surgical workflow recognition,” *Medical Image Analysis*, vol. 73, p. 102158, 2021.
- [37] S. Ramesh, V. Srivastav, D. Alapatt, T. Yu *et al.*, “Dissecting self-supervised learning methods for surgical computer vision,” *arXiv preprint arXiv:2207.00449*, 2022.
- [38] C. I. Nwoye, D. Alapatt, T. Yu, A. Vardazaryan *et al.*, “Cholec-triplet2021: A benchmark challenge for surgical action triplet recognition,” *arXiv preprint arXiv:2204.04746*, 2022.
- [39] M. Pfeiffer, I. Funke, M. R. Robu, S. Bodenstedt *et al.*, “Generating large labeled data sets for laparoscopic image processing tasks using unpaired image-to-image translation,” in *MICCAI*. Springer, 2019.
- [40] W.-Y. Hong, C.-L. Kao, Y.-H. Kuo, J.-R. Wang *et al.*, “Cholecseg8k: a semantic segmentation dataset for laparoscopic cholecystectomy based on cholec80,” *arXiv preprint arXiv:2012.12453*, 2020.
- [41] M. Grammatikopoulou, E. Flouty, A. Kadkhodamohammadi, G. Quellec *et al.*, “Cadis: Cataract dataset for surgical rgb-image segmentation,” *Medical Image Analysis*, vol. 71, 2021.
- [42] D. Alapatt, P. Mascagni, A. Vardazaryan, A. Garcia *et al.*, “Temporally constrained neural networks (tcnn): A framework for semi-supervised video semantic segmentation,” *arXiv preprint arXiv:2112.13815*, 2021.
- [43] D. Owen, M. Grammatikopoulou, I. Luengo, and D. Stoyanov, “Detection of critical structures in laparoscopic cholecystectomy using label relaxation and self-supervision,” in *MICCAI*. Springer, 2021.
- [44] S. M. Strasberg, M. Hertl, and N. J. Soper, “An analysis of the problem of biliary injury during laparoscopic cholecystectomy,” *Journal of the American College of Surgeons*, vol. 180, no. 1, pp. 101–125, 1995.
- [45] P. Mascagni, D. Alapatt, T. Urade, A. Vardazaryan *et al.*, “A computer vision platform to automatically locate critical events in surgical videos: documenting safety in laparoscopic cholecystectomy,” *Annals of surgery*, 2021.
- [46] P. Mascagni, D. Alapatt, A. Garcia, N. Okamoto *et al.*, “Surgical data science for safe cholecystectomy: a protocol for segmentation of hepatocystic anatomy and assessment of the critical view of safety,” *arXiv preprint arXiv:2106.10916*, 2021.
- [47] H. Rezatofghi, N. Tsoi, J. Gwak, A. Sadeghian *et al.*, “Generalized intersection over union,” June 2019.
- [48] T.-Y. Lin, P. Dollár, R. Girshick, K. He *et al.*, “Feature pyramid networks for object detection,” in *Proceedings of the IEEE conference on computer vision and pattern recognition*, 2017, pp. 2117–2125.
- [49] T. Park, M.-Y. Liu, T.-C. Wang, and J.-Y. Zhu, “Semantic image synthesis with spatially-adaptive normalization,” in *CVPR*, 2019.
- [50] R. Zhang, P. Isola, A. A. Efros, E. Shechtman *et al.*, “The unreasonable effectiveness of deep features as a perceptual metric,” in *CVPR*, 2018.
- [51] Z. Wang, A. C. Bovik, H. R. Sheikh, and E. P. Simoncelli, “Image quality assessment: from error visibility to structural similarity,” *IEEE transactions on image processing*, vol. 13, no. 4, pp. 600–612, 2004.
- [52] T. Cai, S. Luo, K. Xu, D. He *et al.*, “Graphnorm: A principled approach to accelerating graph neural network training,” in *ICML*. PMLR, 2021, pp. 1204–1215.